Polymer 145 (2018) 162–173

Contents lists available at ScienceDirect

Polymer

journal homepage: www.elsevier.com/locate/polymer

Polymer crystallinity and crystallization kinetics via benchtop ^{1}H NMR relaxometry: Revisited method, data analysis, and experiments on common polymers

Volker Räntzsch [a], Manuel Haas [a], Mürüvvet B. Özen [a], Karl-Friedrich Ratzsch [a], Kamran Riazi [a], Sandra Kauffmann-Weiss [b], Jordana K. Palacios [c], Alejandro J. Müller [c, d], Iakovos Vittorias [e], Gisela Guthausen [f], Manfred Wilhelm [a, *]

[a] Karlsruhe Institute of Technology (KIT), ITCP, Engesserstr. 18, D-76131, Karlsruhe, Germany
[b] Karlsruhe Institute of Technology (KIT), ITEP, Hermann-von-Helmholtz-Platz 1, D-76344, Eggenstein-Leopoldshafen, Germany
[c] University of the Basque Country (UPV/EHU), POLYMAT and Polymer Science and Technology Department, Faculty of Chemistry, Paseo Manuel de Lardizabal 3, E-20018, Donostia-San Sebastián, Spain
[d] IKERBASQUE, Basque Foundation for Science, E-48013, Bilbao, Spain
[e] LyondellBasell / Basell Polyolefine GmbH, Polymer Physics and Characterization, R&D, Brüningstraße 50, D-65929, Frankfurt, Germany
[f] Karlsruhe Institute of Technology (KIT), MVM, EBI, Pro^{2}NMR, Adenauerring 20b, D-76131, Karlsruhe, Germany

ARTICLE INFO

Article history:
Received 21 February 2018
Received in revised form
17 April 2018
Accepted 26 April 2018
Available online 30 April 2018

Keywords:
Polymer crystallinity
Crystallization kinetics
Semi-crystalline polymers
Low-field NMR
TD-NMR
NMR relaxometry
Molecular dynamics

ABSTRACT

Semi-crystalline polymers play an enormously important role in materials science, engineering, and nature. Two thirds of all synthetic polymers have the ability to crystallize which allows for the extensive use of these materials in a variety of applications as molded parts, films, or fibers. Here, we present a study on the applicability of benchtop ^{1}H NMR relaxometry to obtain information on the bulk crystallinity and crystallization kinetics of the most relevant synthetic semi-crystalline polymers. In the first part, we investigated the temperature-dependent relaxation behavior and identified $T = T_g + 100$ K as the minimum relative temperature difference with respect to T_g for which the mobility contrast between crystalline and amorphous protons is sufficient for an unambiguous determination of polymer crystallinity. The obtained bulk crystallinities from ^{1}H NMR were compared to results from DSC and XRD, and all three methods showed relatively good agreement for all polymers. In the second part, we focused on the determination of the crystallization kinetics, i.e., monitoring of isothermal crystallization, which required a robust design of the pulse sequence, precise temperature calibration, and careful data analysis. We found the combination of a magic sandwich echo (MSE) with a short acquisition time followed by a Carr-Purcell-Meiboom-Gill (CPMG) echo train with short pulse timings to be the most suitable for monitoring crystallization. This study demonstrates the application of benchtop ^{1}H NMR relaxometry to investigate the bulk crystallinity and crystallization kinetics of polymers, which can lead to its optimal use as an *in-situ* technique in research, quality control, and processing labs.

1. Introduction

Since the very beginning of macromolecular science, semi-crystalline polymers such as polyamides, polyesters, and later polyolefins have fascinated generations of scientists because their hierarchical structure spans multiple length scales leading to outstanding toughness, tensile strength, impact resistance, and chemical robustness [1–3]. Furthermore, advantageous optical, electrical, or separation functionalities are oftentimes a direct consequence of the underlying order and crystallinity in materials such as conjugated polymers, dielectrics, or membranes, respectively [4–6]. Controlling the semi-crystalline structure on the level of the nano-, meso-, and macro-scale is the key to achieving the desired final material properties of injection-molded parts, films, or fibers [7]. In contrast to low molecular weight substances, the crystalline structure and habit of polymers are determined not only by the molecular structure, but also by the actual crystallization

* Corresponding author.
E-mail address: Manfred.Wilhelm@kit.edu (M. Wilhelm).

https://doi.org/10.1016/j.polymer.2018.04.066
0032-3861/

conditions [8–10]. Overall, the bulk crystallinity is most affected by these factors as it is sensitive to the molecular weight distribution, chain topology, stereo- and regio-regularity, additives, thermal history, applied pressure, and flow conditions during processing [11,12]. In terms of thermodynamics, the bulk crystallinity of polymers is a process rather than a state function since it is very much path-dependent. Therefore, the kinetics of polymer crystallization are of high interest as a way to understand and control the pathways leading to kinetically trapped states of the material. Polymer crystallization kinetics are comprised of the inherent polymer nucleation and growth rates, which together with the processing conditions (applied flow, temperature, pressure) and selected additives (nucleating agents, fillers, pigments), lead to systems of remarkable complexity [13,14]. The list of established characterization methods that provide information on the structure of semi-crystalline polymers, bulk crystallinity, and crystallization kinetics includes optical and electron microscopy [15], X-ray diffraction (XRD) [16], small and wide angle X-ray scattering (SAXS, WAXS) [17], infrared and Raman spectroscopy [18], differential scanning calorimetry (DSC) [19,20], dilatometry [21], and light scattering [22] to name the most prominent ones. However, most techniques require specific sample dimensions, a special pre-treatment, and do not readily offer online measurement capabilities. The last point is essential as it enables continuous monitoring of polymer crystallization under process-like conditions. Low-field NMR (nuclear magnetic resonance) brings unique advantages as it combines the benefits of a non-destructive characterization method, the versatility of NMR with the potential for *in-situ* experiments of low complexity at affordable prices for a quality or processing lab [23–25]. Further development in the areas of single-sided NMR [26] and hyphenated set-ups [27–29] opened up the field for new possibilities in evaluating multi-phase compositions, chemical reactions, and processes.

A frequently exploited feature that allows for a distinction between multiple phases in ^{1}H NMR is a contrast in molecular mobility, which leads to different linewidths in a spectrum and different relaxation times in a free induction decay (FID). Analyzing decay curves is commonly referred to as NMR relaxometry, a subgroup of NMR experiments in the time domain (TD-NMR). Many materials with mobility contrast have been studied by ^{1}H NMR relaxometry in the past, e.g., fats [30,31], carbohydrates [32], rubbers [33,34], composites [35,36], and also semi-crystalline polymers [37–43]. For food-grade oils and fats these studies have led to industrial standards for the determination of the solid fat content (SFC), which is frequently used for quality control [44,45]. When examining the structurally more complex semi-crystalline polymers, most studies were conducted at high fields with a focus on the decomposition of the FID into multiple components, which is possible due to the high B_0 homogeneities and short NMR probe dead times (<5 μs) [46–51]. However, transverse relaxation of very rigid components is generally so fast that pulse sequences based on solid [52,53] and magic echoes [54–56] are needed to reconstruct the FID in order to obtain information on the initial relaxation behavior of strongly homonuclear dipolar coupled ^{1}H spin systems. The transition to lower fields leads to inherently lower sensitivity and is usually accompanied by lower B_0 homogeneity. A concise quantitative study on the low-field ^{1}H NMR relaxometry of the most commercially relevant semi-crystalline polymers especially with regard to their absolute crystallinity and crystallization kinetics has not yet been published to our knowledge. In addition, a detailed comparison with other established methods such as DSC and XRD helps to validate the applicability of low-field ^{1}H NMR to the study of polymer crystallization. The mobility of polymers is generally temperature-dependent as molecular motion in different domains such as amorphous or crystalline is strongly influenced by the difference between the actual sample temperature and the glass transition temperature T_g. Thus, in the first part of this paper we investigate the temperature-dependent NMR relaxation behavior and identify a minimum relative temperature difference with respect to T_g for which the mobility contrast between crystalline and amorphous protons is sufficient for a determination of the polymer crystallinity. ^{1}H NMR relaxometry results are compared to DSC and XRD results which are based on thermodynamic and structural quantities and are therefore likely to show a certain variation in the discrimination between the crystalline and amorphous fractions. The question is addressed whether low-field ^{1}H NMR relaxometry can be regarded as an absolute method for the determination of the degree of crystallinity X_c or if polymer-specific calibrations are necessary. In the second part, our focus lies on the determination of crystallization kinetics, i.e., monitoring the buildup of crystallinity $X_c(t_{exp})$ during isothermal crystallization. The selection of experimental conditions and data analysis is discussed in detail to serve as a practical aid for other researchers in the field who may in the future consider the use of low-field ^{1}H NMR relaxometry for the measurement of polymer crystallinity and crystallization kinetics.

2. Theoretical basis

2.1. The static limit of homonuclear dipolar coupling

Strong broadening of magnetic resonance lines in the regular crystal lattices of small molecules and polymers was discovered early on by NMR scientists [57–59]. The origin of this effect lies in the dipolar coupling between NMR-active nuclei that are kept at a fixed distance r and are oriented with respect to the static magnetic field B_0 in the absence of molecular motion. In a quantum mechanical approach, the dipolar interaction between two nuclei is represented by a Hamilton operator with the corresponding coupling angular frequency $\Delta\omega(r,\theta)$:

$$\widehat{H}_D^{II} = -\frac{\mu_0 \hbar \gamma_1 \gamma_2}{4\pi r^3} \frac{1}{2}\left(3\cos^2\theta - 1\right)\left\{3\widehat{I}_{1z}\widehat{I}_{2z} - \overrightarrow{\widehat{\boldsymbol{I}_1}} \cdot \overrightarrow{\widehat{\boldsymbol{I}_2}}\right\} \tag{1.1}$$

$$\Delta\omega(r,\theta) = \frac{\mu_0 \hbar \gamma_1 \gamma_2}{4\pi r^3} \frac{1}{2}\left(3\cos^2\theta - 1\right) \tag{1.2}$$

r: distance between two nuclei, γ: magnetogyric ratios (for homonuclear dipolar coupling: $\gamma_1 = \gamma_2$), μ_0: magnetic permeability, $\hbar$: reduced Planck constant, $\widehat{I}$: spin operators, $\widehat{I}_z$: z spin components, θ: angle between the spin pair vector and the static magnetic field B_0.

The cubic dependence on the distance between two nuclei causes a rapid decrease in $\Delta\omega$ for larger values of r and is the reason for the local nature of dipolar interaction (for proton-proton coupling and r in units of Å: $\Delta\omega/2\pi = 122$ kHz/r^3) [60]. Integration over all angles θ leads to the Pake pattern commonly found for strongly coupled isolated spin pairs in solid-state NMR [61]. Hence, a line splitting is observed depending on the orientation of an isolated spin pair in the static magnetic field B_0 (inhomogeneous broadening) [62]. In contrast to the regular crystal lattices of small molecules, polymers are highly complex multi-spin systems (folded chains in unit cells, helical structures, etc.) where multibody interactions between nearby protons that differ in distance and orientation are present leading to distributions in the dipolar couplings. Even though a rigorous treatment is challenging, one can approximate the interactions using only the nearest neighbors due to the local nature of dipolar coupling assuming that the structures

are frozen in a certain conformation. This simplification is applicable to polymers below their T_g and, to a good approximation, to crystalline domains above T_g. For most synthetic polymers, the shortest proton-proton distances are encountered in methylene and methyl groups ($r \approx 1.8$ Å) leading to static couplings of ~21 kHz. The next neighbors in an alkyl chain are ~2.5 Å apart corresponding to a ~7.5 kHz coupling. The Gaussian-broadened sinc-function first suggested by Abragam sufficiently describes the static coupling of spin pairs in the time-domain [63–65]:

$$A(t) = \frac{\sin(2\pi\delta t)}{2\pi\delta t} \times \exp\left[-\left(\frac{t}{T_{2Abr}}\right)^2 \right] \tag{2.1}$$

$$A(t,i) = \sum_i f_i \left\{ \frac{\sin(2\pi\delta_i t)}{2\pi\delta_i t} \times \exp\left[-\left(\frac{t}{T_{2Abr,i}}\right)^2 \right] \right\} \tag{2.2}$$

$\delta = 3/2 \times \Delta\omega/2\pi$: homonuclear Pake anisotropy parameter [60], T_{2Abr}: transverse relaxation time, f_i: weighting factor, t: time.

In Fig. 1, calculated decays based on Equation (2.1) are shown for different values of $\Delta\omega/2\pi$, which are characteristic for an alkyl chain in the absence of molecular motion (a simple model for linear polyethylene below T_g). For more complex structures, decomposition of the measured $A(t)$ into an unknown number of weighted summation terms can be challenging (Equation (2.2)). However, an approximation including only the most dominant interactions and an average Gaussian component is often sufficient to achieve a good representation of the experimental data.

2.2. Molecular dynamics and NMR relaxation

Molecular motion within a polymer becomes more prominent as the temperature is increased, thereby necessitating a theory that incorporates molecular motion into the treatment of dipolar coupling. The stochastic nature of molecular motion leads to an incoherent and therefore irreversible NMR relaxation behavior, which is different from the coherent interaction in the static case of dipolar coupling (dipolar dephasing). A frequently employed theory of NMR relaxation is the BPP model (after Bloembergen, Purcell, Pound) [66] in which time-dependent dipolar coupling fluctuations induced by molecular motion are modeled by the spectral density $J(\omega,\tau_c)$, a Fourier transform of the fluctuating field memory function. The experimentally observed transverse relaxation rate $1/T_2$ is connected to the spectral density $J(\omega,\tau_c)$ by Ref. [67]:

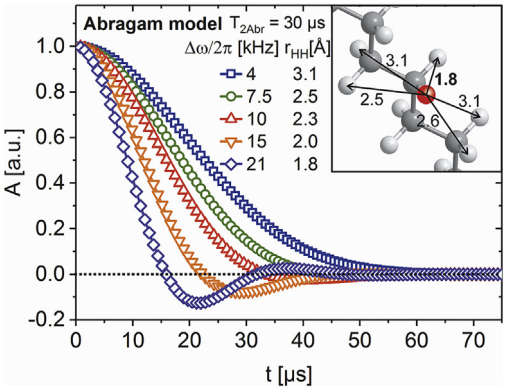

Fig. 1. Calculated decays using a single Gaussian-broadened sinc-function (Abragam model: Equation (2.1)) for various individual spin pair coupling frequencies $\Delta\omega/2\pi$ and corresponding proton-proton distances r_{HH} (Gaussian broadening: $T_{2Abr} = 30$ µs).

$$\frac{1}{T_2} = \left(\frac{\mu_0\hbar}{4\pi}\right)^2 \frac{\gamma^4}{10r^6} I(I+1)[3J(\Delta\omega) + 5J(\omega_L,\tau_c) + 2J(2\omega_L,\tau_c)] \tag{3}$$

r: internuclear distance, γ: magnetogyric ratio, μ_0: magnetic permeability, $\hbar$: red. Planck const., I: spin quantum number (^{1}H: 1/2), $J(\Delta\omega,\tau_c)$: spectral density, $\Delta\omega$: coupling frequency for $T \to 0$ ($\approx$10–20 kHz, secular approx.: $\Delta\omega \approx 0$) [68,69], τ_c: correlation time, ω_L: Larmor frequency.

This concept is strictly applicable only in the motional averaging limit where the time scale τ_c of the motion-induced fluctuating fields is fast compared to the static coupling frequency $\Delta\omega/2\pi$ ($\Delta\omega\tau_c \ll 1$). For polymers, this condition is only fulfilled at temperatures far above T_g. Furthermore, residual dipolar couplings due to anisotropic chain motions might affect the relaxation behavior and lead to intrinsically non-exponential decays, which is not taken into account by the BPP model. For protons with reduced mobility, the BPP model approach for transverse relaxation does not hold and a moment-expansion for the NMR line shape (Anderson-Weiss ansatz [67,70]) gives a better description of the transverse relaxation behavior. Based on the central-limit theorem, the sum of an infinitely large number of random but limited interaction reservoirs is expected to be Gaussian which leads to a Gaussian distribution of the coupling frequencies $\Delta\omega$. For the rigid lattice limit, the time evolution of $A(t)$ is modeled by:

$$A(t) \propto \exp\left[-\frac{1}{2}\left\langle \Omega^2 \right\rangle t^2 \right] \tag{4}$$

$\left\langle \Omega^2 \right\rangle$: second moment of the resonance line shape (in ω), $\left\langle \Omega^2 \right\rangle / 2 \approx 1/T_2$.

At temperatures far above T_g, protons in the center of a polymer crystal are usually rigid with $<\tau_{c,rigid}> \approx 10^{-3}$ s, whereas interfacial protons have an intermediate mobility with $<\tau_{c,intermediate}> \approx 10^{-4}$ s, and amorphous ones are mobile with $<\tau_{c,mobile}> \approx 10^{-6}$ s (exceptions are polymers with pronounced mobility in crystalline domains such as helical flips [60]). As there are rather smooth transitions between phases with different mobilities, choices have to be made with respect to the assignment, i.e., when to call a proton “crystalline”, “interfacial”, or “amorphous” (Fig. 2). This ambiguity can lead to varying results and is one reason for the differences in absolute crystallinity compared to other methods such as DSC, XRD, or microscopy. Each technique measures different physical quantities (heat of fusion, unit cell order, birefringence, etc.) and therefore differences in the crystallinity X_c are also a consequence of the different sensitivity and selectivity towards the crystalline fraction in those techniques.

2.3. Modeling of the transverse magnetization decay and the rigid fraction $\chi(T)$

The selection of a model that accurately describes the transition from static dipolar coupling behavior to relaxation in the rigid lattice limit, and finally to the motional averaging limit is a challenge, especially as static couplings are specific for each polymer. We chose a generalized approach that features a combination of an Abragamian and a Gaussian function to model rigid protons, a Weibullian for intermediately mobile protons ($n = 1.5$), and a mono-exponential for mobile protons (= AGWE model) for the magnetization decay $A(t)$:

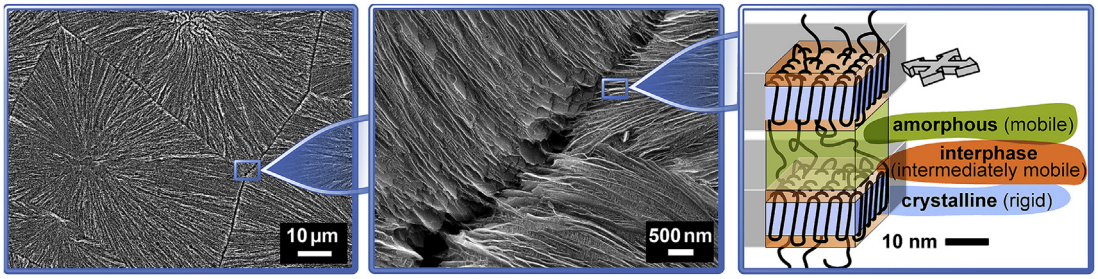

Fig. 2. SEM images of a quiescently crystallized i-PP and schematic lamellar sub-structure with assigned regions of different molecular mobility (recently, Fritzsching et al. [71] showed that chain-folded lamellae display a certain chain tilt to avoid density anomalies). As transitions between the different phases are relatively smooth, choices have to be made with respect to the assignment.

$$A(t) = A_{\mathrm{Abr}}\left\{\frac{\sin(2\pi\delta t)}{2\pi\delta t}\times\exp\left[-\left(\frac{t}{T_{2\mathrm{Abr}}}\right)^2\right]\right\} + A_{\mathrm{G}}\left\{\exp\left[-\left(\frac{t}{T_{2\mathrm{G}}}\right)^2\right]\right\} + A_{\mathrm{Wb}}\left\{\exp\left[-\left(\frac{t}{T_{2\mathrm{Wb}}}\right)^n\right]\right\} + A_{\mathrm{exp}}\left\{\exp\left[-\left(\frac{t}{T_{2\mathrm{exp}}}\right)\right]\right\} \quad (5)$$

Depending on the polymer type the model was simplified to achieve higher numerical stability as will be described in the Results and Discussion section. The temperature-dependent fraction of rigid protons $\chi(T)$ was defined as $\chi(T) = [A_{\mathrm{Abr}}(T) + A_{\mathrm{G}}(T)]/[A_{\mathrm{Abr}}(T) + A_{\mathrm{G}}(T) + A_{\mathrm{Wb}}(T) + A_{\mathrm{exp}}(T)]$ (please be aware of the different notations for the rigid fraction $\chi(T)$ and the degree of crystallinity X_c). The expected temperature-dependence of $\chi(T)$ for an amorphous and a semi-crystalline polymer is shown schematically in Fig. 3. Above T_g one expects a softening phase, leading to a highly mobile material that has sufficient motion to pre-average dipolar coupling for an amorphous polymer at ~ T_g + 50 K according to the Williams-Landel-Ferry (WLF) model of motional activation energies (motions with 0.1/s at T_g are accelerated to ~10^7/s at T_g + 50 K). For semi-crystalline polymers, rigidity is retained in the crystalline domains above T_g, so that $\chi(T)$ becomes a measure of the crystallinity X_c in the plateau region preceding melting (Fig. 3).

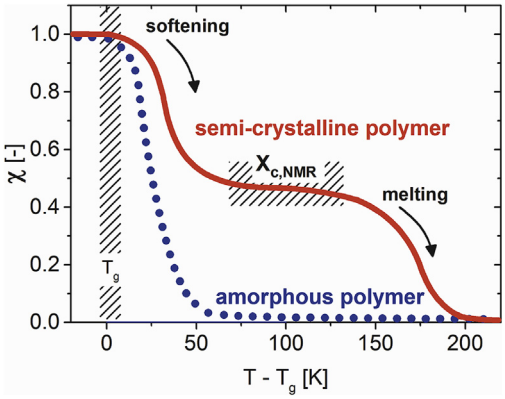

Fig. 3. Scheme illustrating the temperature-dependence of the rigid fraction $\chi(T)$ for an amorphous and a semi-crystalline polymer. The plateau for which $\chi(T) \approx X_c$ is assumed to occur around ~ T_g + 100 K and ends when melting of the polymeric crystals sets in.

2.4. Monitoring of polymer crystallization

Besides measuring the crystallinity of solid samples, monitoring the buildup of crystallinity $X_c(t_{exp})$ from an isotropic melt provides information on crystallization kinetics, which are strongly affected by the chain structure, additives, and processing conditions. Sophisticated decay decomposition tends to be numerically unstable for such a phase transition, and is generally not applicable to magnets of low B_0 homogeneity. The use of a CPMG multi echo sequence (after Carr, Purcell, Meiboom, and Gill) [72,73] is a robust alternative to distinguish between crystalline and amorphous protons. The idea behind this approach proposed by Maus et al. [56] is that only protons of high mobility are captured by the CPMG sequence and these protons can be identified as being amorphous because of the 180° pulse refocusing properties and the chosen duration of relaxation before the first 180° CPMG pulse (τ_{initial}).

Characteristic decays for a super-cooled i-PP melt and after complete isothermal crystallization are given in Fig. 4. To determine evolving crystallinities $X_c(t_{exp})$, two approaches are possible where these methods correspond to the indirect and direct methods for the SFC determination of fats [44,45]. We refrain from a sophisticated decay decomposition as the method should be applicable to any magnet independent of B_0 homogeneity.

Direct method. For every point in the experimental/crystallization time (t_{exp}), CPMG intensities $I_{CPMG}(t_{exp})$ are back-extrapolated

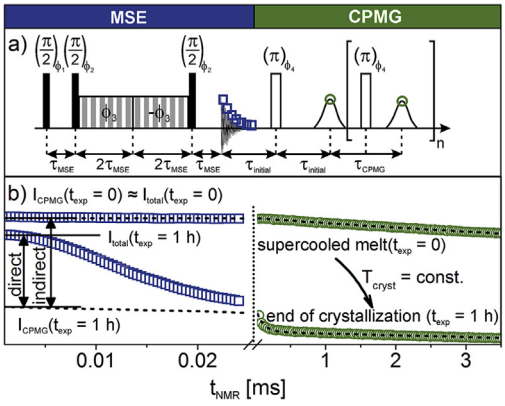

Fig. 4. (a) ^{1}H NMR pulse sequence proposed by Maus et al. [56] based on a mixed magic sandwich echo (MSE) to refocus the signal of a strongly homonuclear dipolar coupled spin system, and a CPMG sequence to selectively detect mobile protons. (b) MSE (open squares) and CPMG data (open circles) for a super-cooled i-PP melt (t_{exp} = 0 h) and at the end of isothermal crystallization (t_{exp} = 1 h). Either a direct or indirect data processing approach similar to the SFC determination of fats [44,45] can be chosen to study the buildup in crystallinity $X_c(t_{exp})$.

to $t_{NMR} = 0$ ms and compared with the total intensity $I_{total}(t_{exp})$ at $t_{NMR} = 0$ ms of all protons as captured by the mixed magic sandwich echo:

$$X_{c,direct}(t_{exp}) = \frac{C \times I_{CPMG}(t_{exp})}{I_{total}(t_{exp})} \quad (6.1)$$

This approach is applicable for both iso- and non-isothermal protocols because the overall change in signal intensity during crystallization is directly detected (e.g., change in temperature, slight detuning of the NMR probe, drift of the magnet, etc.). However, the echo sequences employed to capture all protons (I_{total}) are prone to errors if motions within the solid are on the time scale of the refocusing pulses blocks such as chain flips in polyethylene [74–76]. As by definition the degree of crystallinity $X_{c,direct}(t_{exp})$ has to be zero for the super-cooled melt at $t_{exp} = 0$ min, a correction factor $C = I_{total}(t_{exp} = 0\,\text{min})/I_{CPMG}(t_{exp} = 0\,\text{min})$ is needed where this factor depends on the B_0 homogeneity, MSE performance, and fitting uncertainties.

Indirect method. In contrast to the direct method, CPMG intensities $I_{CPMG}(t_{exp})$ are back-extrapolated to $t_{NMR} = 0$ ms and compared with the back-extrapolated CPMG intensity at $t_{exp} = 0$ min at which the sample was in a super-cooled melt state at T_{cryst}:

$$X_{c,indirect}(t_{exp}) = 1 - \frac{I_{CPMG}(t_{exp})}{I_{CPMG}(t_{exp} = 0)} \quad (6.2)$$

The indirect approach is applicable to isothermal protocols and to polymers with a significant crystal mobility (e.g., HDPE, LDPE, PEO) because it only relies on the decreasing CPMG intensities. It can be used to analyze and compare data acquired on various magnet types as the CPMG sequence is more robust against gradients in B_0 than the magic sandwich echo sequence [77]. Fitting uncertainties, systematic fitting errors, and changes in the NMR sensitivity can be accounted for by introducing a correction term to Equation (6.2). However, since the main goal of isothermal crystallization experiments is to obtain information on the crystallization kinetics, the analysis is usually performed on relative crystallinities $X_{c,NMR}/X^{\infty}_{c,NMR}$ and their volume-related counterparts $\phi_{c,NMR}/\phi^{\infty}_{c,NMR}$, which does not require a correction or calibration (similar to isothermal DSC experiments as shown in the Results and Discussion Section).

The direct and indirect methods require the careful selection of pulse timings for the CPMG sequence and a delay between the MSE and CPMG segments to achieve high fit stability and an accurate determination of the amorphous fraction. The echo timing is desired to be as short as possible in order to provide a sufficiently large number of data points and is mainly limited by the acquisition time, the probe dead time, and the 180° pulse length. The lowest possible values for τ_{CPMG} are on the order of 20–30 μs for commercial solid state low-field probes. To quantitatively detect all mobile protons with the CPMG sequence, we propose the use of a short MSE recording interval ($\tau_{inital} = 25$ μs) during which only the signal that originates from rigid protons is decaying. This ensures that protons with intermediate mobility are captured as a fast decaying component in the CPMG part.

3. Experimental

3.1. Materials

Molecular weights, polydispersities, glass transitions temperatures, peak melting temperatures, and crystallinities for all polymers as determined by DSC and XRD are given in Table 1. The samples contained standard anti-oxidants, but no nucleating agents. Polyamide 6 (PA-6) and polyethylene terephthalate (PET) were dried at 70 °C under vacuum for 7 days to remove residual moisture. Tacticity of both polypropylenes was determined by ^{13}C NMR to be ~94% *mmmm*. Sample i-PP-2 contained ~1 mol% of 2,1-erythro regio defects leading to γ-form crystallization and a higher nucleation density than for i-PP-1, which crystallized in the α-form.

3.2. NMR equipment and experimental details

All ^{1}H NMR experiments were performed on a Bruker "the minispec" mq20 (Bruker BioSpin GmbH, Rheinstetten, Germany) with $B_0 = 0.5$ T at 39.5 °C ($\omega_L/2\pi = 20$ MHz for ^{1}H) and a ~4 ms FID for a silicone oil. The sample temperature was controlled by a Bruker Variable Temperature (BVT) unit operated with pressurized air and a flow rate of 1200 l/h. The NMR probe characteristics were: dead time ~10 μs, pulses 2.6 μs (p_{90}), 5.1 μs (p_{180}) for 0 dB pulse attenuation, and bandwidth ~500 kHz FWHM.

For the temperature-dependent experiments, mixed magic sandwich echo (MSE) decays of 100 μs were recorded with $\tau_{MSE} = 4\tau_{\phi} + 4.5p_{90}/2 = 15$ μs where $\tau_{\phi} = 2.2$ μs (optimized for maximum signal intensity and phase coherence). All data were accumulated (16 scans) with a 3.5 s recycle delay and phase cycling: $\phi_1 = x\bar{x}x\bar{x}$, $\phi_2 = \bar{y}y\bar{y}y$, $\phi_3 = x\bar{x}x\bar{x}$, $\phi_4 = y\bar{y}y\bar{y}$, $\phi_{rec} = x\bar{x}x\bar{x}$. On-resonance was ensured for all experiments and the phase was adjusted using a zero order phase correction. Only the real part was selected for analysis of the decay decomposition. In all crystallization experiments, a combination of a MSE decay ($\tau_{initial} = 25$ μs) and a succeeding CPMG echo train ($\tau_{CPMG} = 25$ μs) with phase cycling was employed. Details on the MSE pulse sequence can be found in the works by Takegoshi et al. [54], Demco et al. [55], and Maus et al. [56]. Approximately 20–30 polymer pellets (in total ~1 cm^3) were put into 10 mm borosilicate glass NMR tubes, which were purged a couple of times with Argon, evacuated, and finally sealed to reduce convection and oxidative degradation.

3.3. Further characterization techniques

High-temperature gel permeation chromatography (HT-GPC) at 145 °C was done using trichlorobenzene as the eluent for i-PP, HDPE, and LDPE. Standard GPC at room temperature was performed using respective calibration standards for t-PI and PS in tetrahydrofuran, and for PET and PA-6 in hexafluoroisopropanol. Isothermal and non-isothermal differential scanning calorimetry (DSC) were performed on a Mettler DSC30 with a TC15 temperature controller and a liquid nitrogen cooling unit (Mettler-Toledo GmbH, Gießen, Germany). The temperature profile for isothermal crystallization experiments was: RT to $T_{isomelt}$ at 10 K/min, hold at $T_{isomelt}$ for 12 min, $T_{isomelt}$ to T_{cryst} at −60 K/min, hold at T_{cryst} for 2–3 h where $T_{isomelt}$ was set to +40 K above the peak maximum temperature of the respective DSC melting endotherms and T_{cryst} was chosen to yield complete crystallization within the given time interval of 2–3 h. X-ray diffraction (XRD) experiments were carried out on a Bruker D8 Discover (Bruker AXS GmbH, Karlsruhe, Germany) with a Cu X-ray tube (40 kV, 40 mA), Göbel mirror, an Anton Paar HTK1200 N heating chamber (Anton Paar, Graz, Austria), a 0.2 mm Soller slit, and a LYNXEYE XE detector (0D mode). Prior to all experiments, the z-position of the sample was scanned and adjusted for the respective sample dimensions. The diffractograms were acquired by continuous scanning between $2\theta = 5$–34° first at 30 °C, then at elevated temperatures of +40 K above the peak maximum melting temperature observed in non-isothermal DSC experiments, and finally again at 30 °C after cooling from the melt at approximately −10 K/min. The heating chamber was evacuated

Table 1
Molecular weights, polydispersities (GPC), glass transition temperatures (lit.) [1,2], peak melting temperatures (DSC), and crystallinities (DSC/XRD) for all polymers investigated.

Polymer	Supplier	M_w [kDa]	$Đ_M$ [-]	T_g [°C]	T_m [°C] neat	T_m [°C] def.	$X_{c,DSC}$* neat	$X_{c,DSC}$* def.	$X_{c,XRD}$‡ neat	$X_{c,XRD}$‡ def.
HDPE	LyondellBasell	182	11	−120	135	134	0.61	0.65	0.52	0.63
LDPE	LyondellBasell	135	11	−120	112	111	0.43	0.45	0.45	0.45
i-PP-1	Repsol	246	2.7	−10	168	165	0.44	0.54	0.45	0.54
i-PP-2	LyondellBasell	202	1.9	−10	161	158	0.44	0.48	0.49	0.48
PA-6	BASF	61.8	2.1	+40	226	222	0.62	(-)†	(0.58)	(-)†
PET	Invista	50.2	2.0	+70	261	259	0.36	0.49	0.40	0.47
t-PI	Sigma Aldrich	129	4.6	−60	65	63	0.33	0.30	0.37	0.39
PS	Sigma Aldrich	209	1.9	+105	N/A	N/A	N/A	N/A	N/A	N/A

(*) Heats of fusion ΔH_u were determined by integration of DSC melting endotherms (avg. of 3 runs, 10 K/min heating rate) for neat pellets and upon defined cooling at −10 K/min from the melt ("def."). Respective crystallinities $X_{c,DSC}$ were obtained by a comparison with theoretical values for $\Delta H_u(X_c = 1)$ [1]. (†) Degradation was observed after heating up to 300 °C. (‡) XRD diffractograms were recorded for ~5–10 pellets first at 30 °C, then at elevated temperatures (fully molten), and finally at 30 °C after defined cooling at −10 K/min from the melt ("def."). The integrated diffractograms were compared to obtain the respective crystallinities $X_{c,XRD}$. See the Results and Discussion Section and Supporting Information for plots and additional information.

to reduce X-ray background scattering and polymer degradation. XRD data processing was performed using Bruker DIFFRAC. EVA (Bruker AXS GmbH, Karlsruhe, Germany).

4. Results and discussion

4.1. Crystallinity of solid samples

Mixed magic sandwich echoes (MSE) were recorded for all samples over a large temperature interval to study the transition from a fully rigid state below T_g to a state of increased softness above T_g, and finally to a highly mobile melt state (Fig. 5). All datasets were normalized to the MSE maximum in order to remove the effect of inherently different intensities based on the Boltzmann population of spin states. The polymers investigated in this study contain different functional groups, e.g., methylene, methyl, or phenylene units. Hence, in the static case of dipolar coupling, multiple proton-proton dipolar couplings are present and

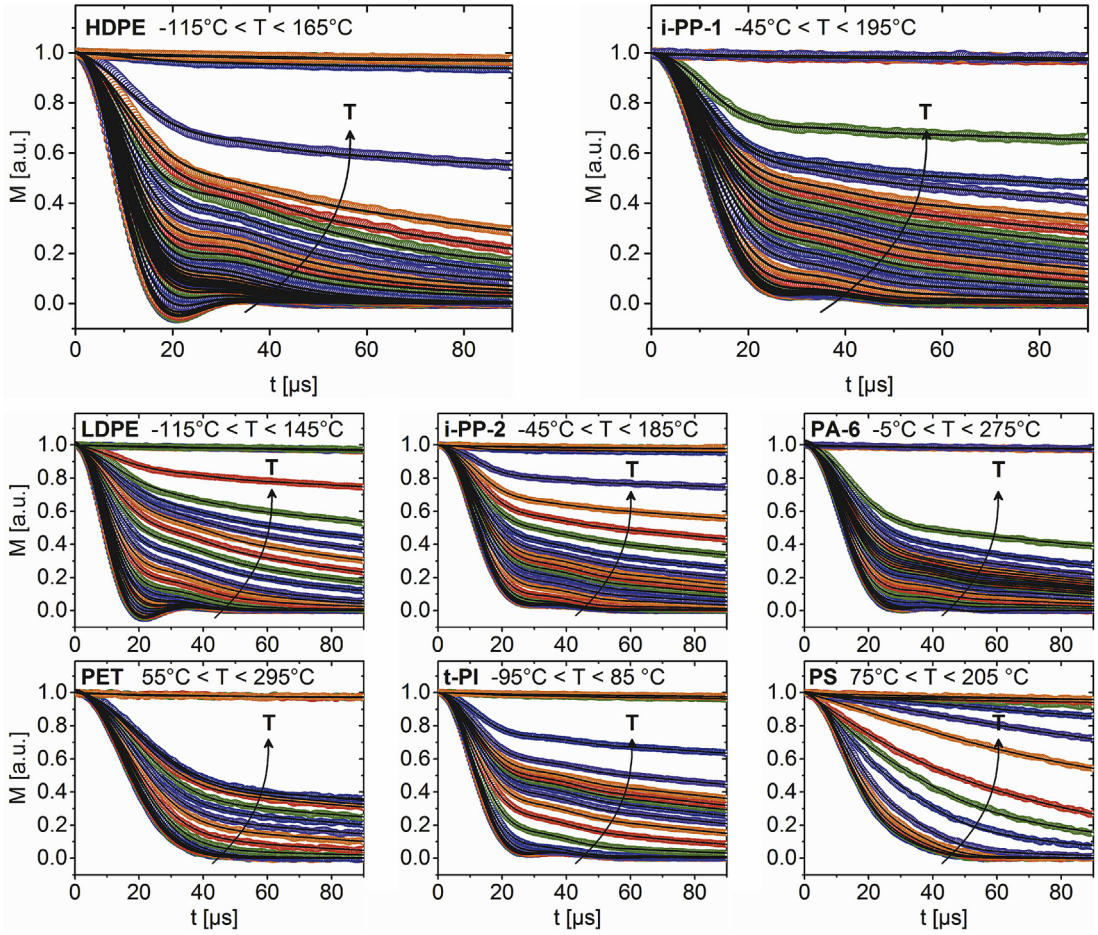

Fig. 5. Temperature-dependent normalized mixed magic sandwich echo (MSE) decays for different polymers. Strong static coupling was observed for HDPE and LDPE, whereas for i-PP, PA-6, and t-PI there was only a plateau-like decay in the region of 20–50 µs detected even below T_g. PS and PET showed a Gaussian decay without an oscillation. The black lines represent the fitted model and describe the curves well over the large temperature range (Equation (5), $\delta = 30$ kHz, T_{2Abr}: free parameter with values of ~20–30 µs, T_{2G}: free parameter with values of ~30–50 µs, T_{2str}: free parameter with values of ~30–50 µs, $n = 1.5$, T_{2exp}: free parameter with values of ~50–500 µs).

consequently different patterns were observed at temperatures below and close to T_g. All polymers shared the feature that they show rapid decays to zero within ~50 μs after the creation of the mixed magic sandwich echo at the lowest measured temperatures, which is a consequence of the high rigidity and absence of strong segmental motion below T_g. A pronounced oscillation between 20 and 50 μs was observed for the polyethylenes (HDPE, LDPE) and this was likely provoked by dominating Pake-type interactions between coupled methylene protons. The data for all other polymers displayed less distinct oscillations and almost monotonically decaying curves, which were a result of the less defined dipolar network and an effective summation of multiple coupling terms. With increasing temperature, a slowly decaying component appeared that originated from the increasing mobility in the amorphous and interfacial regions due to segmental motion. The strong oscillation at low temperatures over the time interval of 20–50 μs transformed into a plateau-like behavior with increasing temperature. For all polymers, the Gaussian-type initial decay vanished gradually with increasing temperature. For the amorphous polystyrene (PS), a step-wise change from Gaussian to exponential behavior was observed with intermediate motional decay shapes originating from increased segmental motion and dynamic heterogeneities. Ultimately, at temperatures above the nominal melting points, an almost straight line was observed on the time scale of a few tens of μs, which reflected the T_2^* relaxation dominated by the B_0 homogeneity.

The MSE decays were analyzed by applying a combined model (Equation (5)) to the initial 100 μs after the creation of the mixed magic sandwich echo to extract information on the fractions of rigid, intermediately mobile, and mobile protons (black lines in Fig. 5). Compared to the spectral line fitting at high fields using phenomenological Gaussian or Lorentzian functions, this approach was found to be more precise. As all polymers contain methylene groups, a dedicated Abragamian with $\delta = 30$ kHz and T_{2Abr} as a free parameter (~30–50 μs) was chosen to account for the strong oscillations and plateau-like behavior observed in the data. With its simple repeat unit consisting only of methylene protons and a regular zig-zag conformation in a polymer crystal, polyethylene presents a special case that does not require the additional Gaussian component to achieve an accurate representation of the data (= A(G)WE). Due to the higher structural complexity of the other polymers and the associated multiple couplings, an additional Gaussian component was necessary to numerically describe the relaxation behavior sufficiently well for i-PP, PA-6, PET, t-PI, and PS. During the analysis it was found that the Weibullian component could be set to zero for these polymers while still providing a good representation of the data and with the benefit of less free parameters (= AG(W)E). This somewhat arbitrary decision marks a limit of the analysis: for polymers with a more complex repeat unit than polyethylene, the domains of intermediately mobile and rigid protons as indicated in Fig. 2 cannot be clearly separated by the selection of one or two dedicated Abragamians and a Weibullian. Therefore the reduction to a simplified two-phase model (rigid + mobile) was necessary to achieve high numerical fit stability.

In Fig. 6, the temperature dependence of the rigid proton fraction $\chi(T)$ is shown for all polymers. Below T_g the curves exhibit a plateau ($\chi(T) = 1$) that ends shortly above T_g when increased molecular motion led to a softening of the amorphous part of the material. For the amorphous PS sample, a single softening phase was observed as $\chi(T)$ effectively decayed to zero for $T \approx T_g + 50$ K, which agreed with the expected WLF activation behavior of molecular motion in amorphous polymers. Depending on the specific type of semi-crystalline polymer, the initial softening phase extended until $T \approx T_g + 100$ K where another plateau was observed

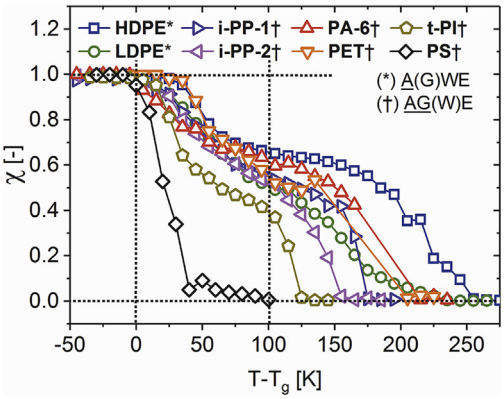

Fig. 6. Temperature-dependence of $\chi(T)$ for different semi-crystalline polymers and amorphous polystyrene. At $T \approx T_g + 100$ K, a plateau-like behavior was observed for all semi-crystalline polymers defining the temperature interval over which there is sufficient mobility contrast between the amorphous and crystalline protons to determine $X_{c,NMR}$ using the chosen decomposition approach. Melting set in at relatively low $T - T_g$ values for t-PI, i-PP-2, and LDPE and $\chi(T)$ decreased soon after reaching the short plateau around $T \approx T_g + 100$ K for these polymers.

thereby marking the region over which the mobility contrast between crystalline and amorphous protons is sufficient for a determination of X_c using the applied MSE decomposition method. Notably, the temperature that was required to reach a plateau for all semi-crystalline polymers in Fig. 6 did not exactly coincide with the mobile plateau $\chi(T) = 0$ for the purely amorphous polystyrene (PS), which suggests that some rigidity is retained, i.e., through linkages of amorphous chains to crystalline domains or additional local physical constraints that shifted the activation barrier of the underlying motions to higher values and therefore higher temperatures. Presumably, this effect is closely related to a boundary layer of immobilized chain segments at the surface of lamellar crystals (rigid amorphous fraction of intermediate mobility). With a further increase in temperature, melting started and led to a value of $\chi(T) = 0$ when the samples were fully molten. Since the samples investigated here were neat pellets in a non-equilibrium state, it is very likely that there were many small crystallites and thin lamellae present in the samples which caused melting at comparably low temperatures (see Supporting Information for DSC heating traces). For all polymers except of t-PI, the onset of melting occurred after the plateau at $T \approx T_g + 100$ K was reached. Melting of the neat t-PI sample set in around $T_g + 100$ K, which was in accordance with DSC. The mixed magic sandwich echo sequence used in the experiments here performed better than a simple solid echo to quantify the total proton amount. However, it was still not able to perfectly refocus all magnetization possibly due to gradients in B_0 and the resulting distribution of pulse lengths (10% signal reduction compared to a FID). Furthermore, for temperatures at which motional modes have a comparable time scale to the refocusing block duration, the magic sandwich echo intensity decreased significantly (for ~ $T_g + 50$ K for segmental motion of amorphous chains and ~$T_g + 200$ K for helical flips of crystalline chains). However, at this stage there was no alternative to the mixed magic sandwich echo, and the overall trends agreed with solid-state NMR experiments carried out at high field. The values of $\chi(T)$ at $T = T_g + 100$ K were chosen as a measure of crystallinity $X_{c,NMR}$ for further interpretation. A relative error of ±10% was estimated, mainly given by fitting uncertainties over the time interval of 20–50 μs and assuming a certain ambiguity in the assignment of crystalline vs. amorphous protons that had an intermediate mobility.

In the following discussion, crystallinities X_c determined by NMR are compared with DSC and XRD results. DSC heating traces

of "as received" pellets (10 K/min heating rate) were integrated and compared with literature values for theoretically 100% crystalline samples [1]. An example of such a melting endotherm is given for i-PP-1 in Fig. 7a (see Supporting Information for additional data). An average of three samples was determined with a relative error of approximately ±10%, which was potentially caused by different cooling conditions for each pellet during processing and the inherent experimental error. Main sources of uncertainty in DSC are the selection of integration limits, setting of the baseline, and the literature values for theoretically 100% crystalline samples.

XRD diffractograms were recorded for "as received" pellets at room temperature and at a temperature above the nominal melting point to obtain information on the amorphous halo shape. The amorphous halo was adjusted in the vertical and horizontal directions to match the minima of the measured diffractograms at room temperature. Fig. 7b shows the results for i-PP-1 with the black line representing the shifted amorphous halo. A comparison of the integrals yielded the XRD crystallinity. This method was found to be more appropriate for semi-crystalline polymers than a simple Gaussian fit because the amorphous halo is not necessarily symmetric and its shape depends on the polymer type and apparatus. Generally, the sources of error in the XRD measurements are the estimation of the amorphous halo, the selection of integration limits and the baseline, and angle-dependent intensity/angle shifts when a Bragg-Brentano geometry is used for samples that are not perfectly flat.

In Fig. 8, a comparison of crystallinity values X_c determined by DSC, XRD, and NMR is shown for all investigated semi-crystalline polymer types. The obtained values agreed relatively well within the estimated experimental errors of ±10%. As described in the introduction, each characterization technique measures a different physical quantity (heat of fusion, unit cell order, birefringence, etc.). Hence, the structural assignment to crystalline, interfacial, and amorphous domains varied based on the different length and time scales involved in the measurements. For the NMR experiments, the selected model and data analysis method were found to be a good compromise between an accurate description of the data and high numerical fit stability. At temperatures of $T \geq T_g + 100$ K, the mobility difference between amorphous and crystalline protons was sufficient for a determination of polymer crystallinity.

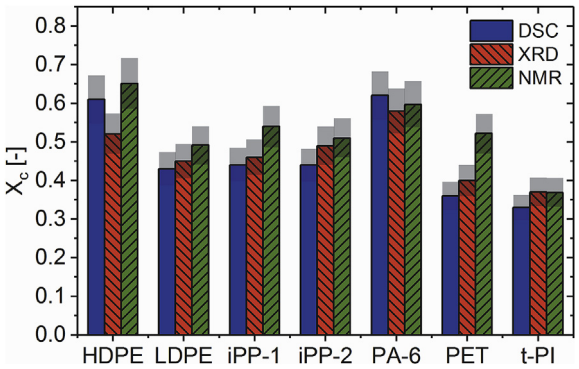

Fig. 8. Comparison of crystallinities X_c for different polymers as determined by DSC, XRD, and NMR. The methods agreed rather well within an estimated relative error of ±10% (indicated in grey), which could be attributed to experimental uncertainties (temperature control, sensitivity, etc.) as well as to the data analysis (baselines, integration ranges, data fitting models, etc.). $T = T_g + 100$ K was found to be the lowest suitable temperature for measuring the crystallinity by NMR relaxometry as this was the lower limit where there was a sufficient mobility difference between the amorphous and crystalline protons.

4.2. Monitoring polymer crystallization and crystallization kinetics

The buildup of the degree of crystallinity as a function of time during polymer crystallization was studied for all polymers listed in Table 1 except for PET as the temperatures needed for slow crystallization (>230 °C) exceeded the specifications of the NMR probe. For all other polymers, crystallization temperatures were chosen to achieve complete crystallization within a 1–2 h time frame. This constraint resulted in crystallization temperatures far above T_g for the polyethylenes (HDPE: T-$T_g \approx 245$ °C, LDPE: T-$T_g \approx 225$ °C), where only a low absolute crystallinity was obtained even for very long crystallization times (post-crystallization occurred when the samples were cooled down to room temperature). For the other polymers, the crystallization temperatures were closer to the observed plateau in $\chi(T)$, and higher absolute crystallinities were consequently achieved. As the main purpose of these crystallization experiments is to extract information on the kinetics rather than the absolute crystallinity, a comparison was drawn based on the time evolution of the relative crystallinities.

In Fig. 9a, an isothermal crystallization experiment for i-PP-1 at $T_{cryst} = 136$ °C is shown. The initial MSE decay exhibited the

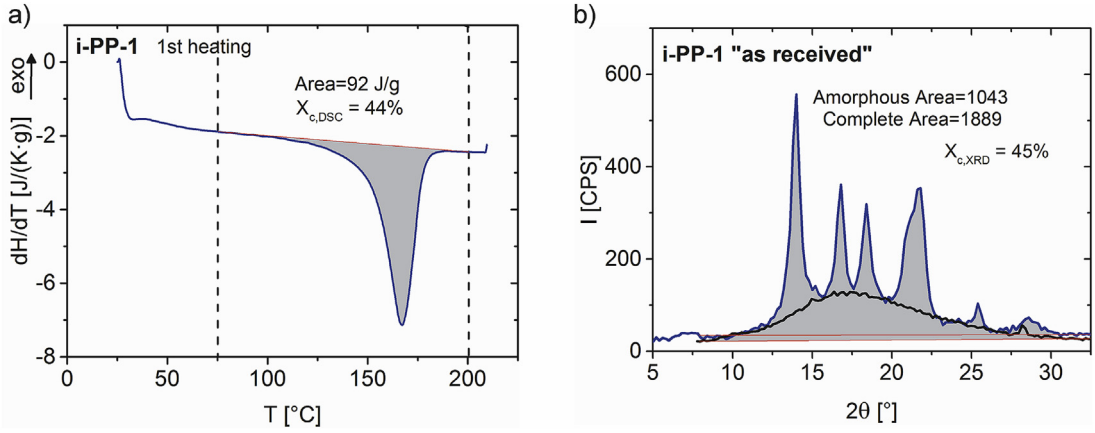

Fig. 7. (a) DSC heating trace of i-PP-1 ("as received" pellets) recorded at 10 K/min. Integration of the melting endotherm and comparison with literature values for a theoretically 100% crystalline sample yielded a DSC crystallinity of 44%. (b) XRD diffractogram of i-PP-1 at 30 °C (blue line) and a shifted amorphous halo (black line) recorded at 200 °C. A comparison of the integrals for $7.5° < 2\theta < 30°$ yielded an XRD crystallinity of 45% (additional data in the Supporting Information). (For interpretation of the references to colour in this figure legend, the reader is referred to the Web version of this article.)

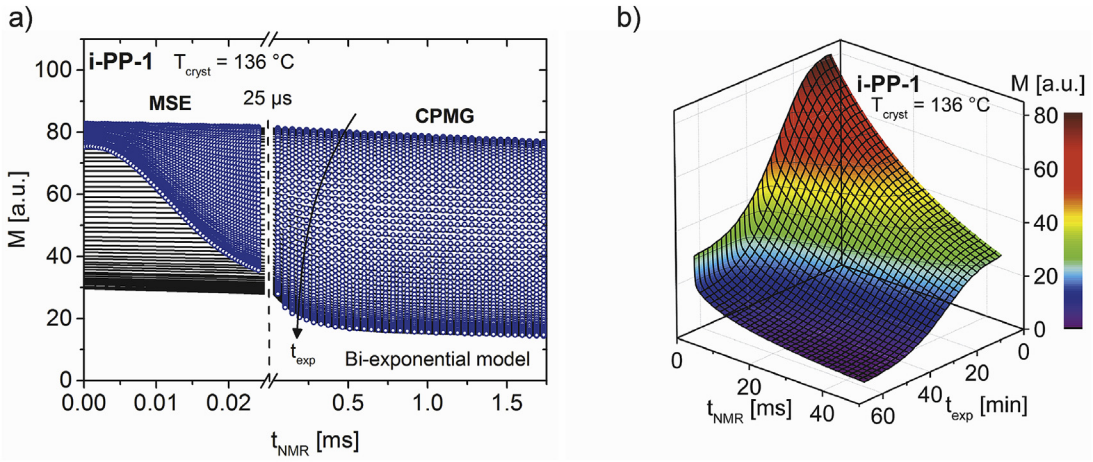

Fig. 9. Isothermal crystallization of i-PP-1 at 136 °C as monitored by a MSE-CPMG sequence. (a) Evolution of the decays and bi-exponential fits to the CPMG data (1.75 ms shown; black lines are back-extrapolations to $t_{NMR} = 0$ ms). (b) Waterfall plot of the CPMG decays during crystallization. The CPMG intensity at $t_{NMR} = 0$ ms displays the expected inverse S-shape, which was caused by an effective loss of magnetization due to the conversion of amorphous to crystalline protons during crystallization.

formation of a Gaussian decay with progressing crystallization. Consequently, the CPMG decays were reduced in intensity and transformed from slow mono-exponential into bi-exponential decays that incorporated relaxation contributions from protons of high and intermediate mobility. Since in the applied CPMG sequence the pulse phases were kept constant during the echo train, partial spin-locking might have led to a $T_{1\rho}$ relaxation contribution. This effect could be reduced by applying phase cycles such as MLEV-4 or XY-16 if one wants to analyze the full echo train in terms of the true T_2 time evolution during crystallization. However, complex phase cycles are not readily applicable to systems of low B_0 and B_1 field homogeneity, which were aimed at in the work presented here. Furthermore, the intensity ratio between rigid and amorphous components was found to be independent of the respective relaxation times. The evolution of CPMG data in "experimental" and "NMR" time revealed the inverse S-shape for the decline in CPMG intensity caused by an effective decrease of mobile protons during crystallization (Fig. 9b). The CPMG data was modeled with a bi-exponential over the range of 0.05–10 ms to extract information on the amorphous fraction.

As pointed out in the introduction, NMR crystallization data can be analyzed in a direct or indirect way that is conceptually similar to the SFC determination of fat composites [44,45]. Back-extrapolated CPMG intensities ($t_{NMR} = 0$ ms) characterizing the amorphous fraction can either be compared directly to the MSE maximum at each point in experimental/crystallization time t_{exp}, or indirectly to the super-cooled melt signal at $t_{exp} = 0$ min (Equations (6.1)–(6.2)). Results of the different data analyses methods for the crystallization experiment in Fig. 9 are shown in Fig. 10a. The shapes were very similar and the final plateaus differed only slightly depending on the data processing method. The observed scattering of $X_c(t)$ was almost identical and was mainly due to the fit stability. It was found that a short echo time ($\tau_{CPMG} = 25$ µs) and short MSE duration ($\tau_{initial} = 25$ µs) drastically improved the fit quality as the fast relaxing amorphous component could only be modeled accurately when a sufficient number of echoes was recorded during the initial 200 µs? For the polyethylenes the MSE intensity decreased significantly at the respective crystallization temperatures, potentially due to 180° chain flips acting on the time scale of the MSE refocusing blocks [75,76]. The indirect method, based only on the CPMG part, offered a more robust way to obtain crystallinities as it is independent of the MSE efficiency. NMR and DSC results for isothermal crystallization experiments of i-PP-1 carried out at different temperatures are compared in Fig. 10b. Since isothermal DSC experiments cannot readily be integrated to yield absolute values, relative crystallinities were compared with respect to their curve shapes and associated kinetics. The trend of slower crystallization with increasing crystallization temperature for $T_{cryst} > (T_m^0 + T_g)/2$ was well captured by both techniques. The DSC data exhibited a slightly more symmetric S-shape, i.e., a later onset but higher slope at the turning point, which was probably a result of the smaller sample volume (~20 mm^3) and therefore lower temperature gradient relative to NMR (~1 cm^3 sample volume).

In Fig. 11, isothermal crystallization curves measured at different temperatures are shown for the investigated polymers. The trend "higher crystallization temperature leads to slower crystallization" for $T_{cryst} > (T_m^0 + T_g)/2$ was seen for all polymers. Over the investigated temperature intervals, the results for the polyethylenes showed the strongest dependency on the crystallization temperature. The immediate increase in relative crystallinity for the polyethylenes upon reaching the crystallization temperature was presumably caused by a temperature gradient of ~1 K within the sample volume of ~1 cm^3 (see Fig. 11 and compare with kinetic crystallization data obtained by isothermal DSC experiments in the Supporting Information). A substantial temperature gradient should show the strongest effect on the kinetics of the high-density and low-density polyethylene samples, as their growth rates are highly sensitive to even the smallest crystallization temperature differences ($\Delta T = 1$ °C ≙ factor of 2 in the growth rate) over the chosen crystallization temperature intervals of $T_{cryst} = 124$–126 °C and 102–105 °C, respectively. All curves were fitted using a volume-based Avrami model [78] up to 50% relative crystallinity to obtain the kinetic rate K and the exponent n:

$$\frac{\phi_c(t)}{\phi_c^\infty} = 1 - \exp\{-[K(t - t_0)]^n\} \tag{7.1}$$

$$\phi_c(t) = \frac{\rho_a}{\frac{\rho_c}{X_c(t)} + \rho_a - \rho_c} \tag{7.2}$$

ϕ_c: volume crystallinity, ϕ_c^∞: final volume crystallinity, K: Avrami rate, n: Avrami exponent, t: time, t_0: induction time, X_c: mass crystallinity, ρ_a, ρ_c: density of the fully amorphous and crystalline materials (lit.) [2].

The curves for the two i-PPs, PA-6, and t-PI were well described by the Avrami fit over the range of $0 < \phi_c/\phi_c^\infty < 0.5$. As

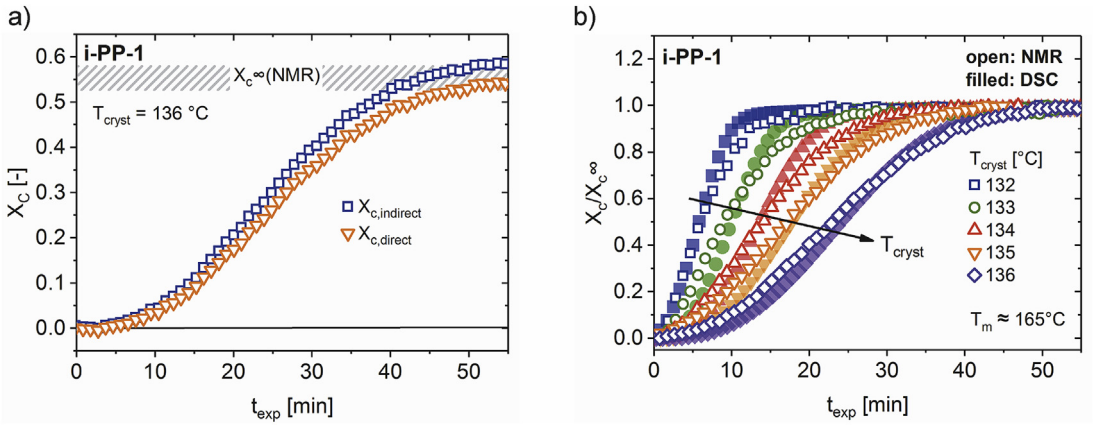

Fig. 10. (a) Comparison of the direct and indirect NMR data analysis methods. The different methods yielded similar values with a final crystallinity of $X_{c,NMR}^{\infty} \approx 57 \pm 2\%$. (b) Isothermal crystallizations of i-PP-1 at different temperatures as determined by NMR (indirect data analysis) and the corresponding DSC experiments. The NMR data matches the DSC curves well.

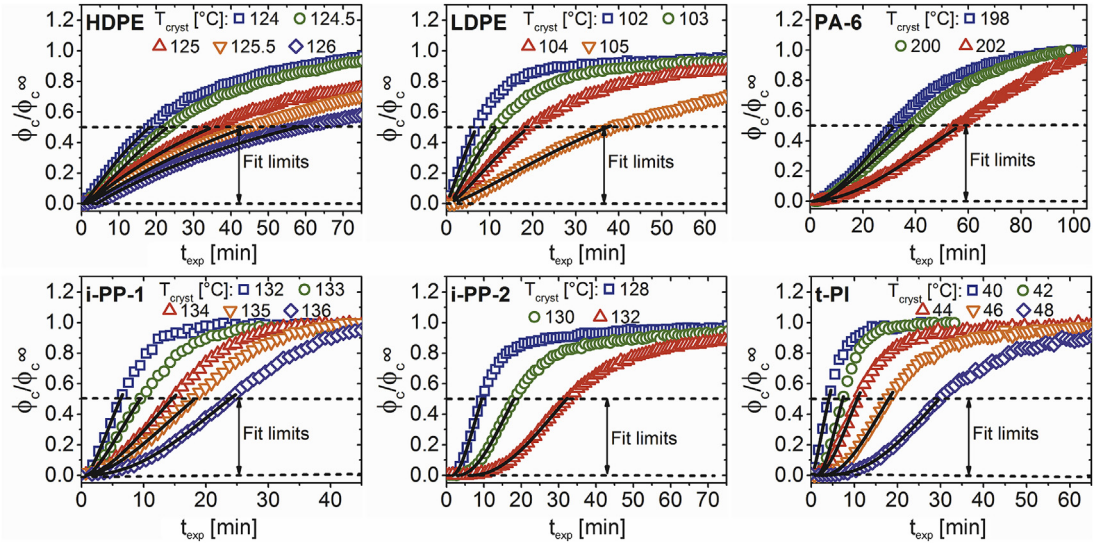

Fig. 11. Isothermal crystallization traces for several different polymers and their crystallization temperatures (indirect data analysis). All curves exhibit the trend "higher crystallization temperature leads to slower crystallization" which is usually observed for $T_{cryst} > (T_m^0 + T_g)/2$. The immediate increase in the relative crystallinity of HDPE and LDPE upon reaching the crystallization temperature was most certainly caused by a temperature gradient in the sample. All curves were fitted using an Avrami model up to 50% relative crystallinity to obtain the kinetic rate K and the exponent n.

the Avrami model does not account for growth rate distributions, it is strictly valid only in the absence of a temperature gradient, which is experimentally difficult to achieve for the sample volume of ~1 cm^3 in the NMR probe we currently use. When compared to the K and n values obtained from isothermal DSC experiments, the Avrami rate K measured by NMR showed a high level of agreement for each polymer (Fig. 12). The Avrami exponent n extracted from DSC experiments deviated somewhat from the values determined by NMR. The origin of this discrepancy is presumably the aforementioned temperature gradient of ~1 °C across the sample in the NMR experiments, which led to a distribution in the growth rate K and therefore an apparently lower n value (see Supporting Information for the decreasing effect of a growth rate distribution on the exponent n). By optimizing the temperature control and NMR probe design, a reduction in the temperature gradients and a closer match to DSC data is likely to be achieved.

5. Conclusions

In the present paper, we investigated the applicability of benchtop ^{1}H NMR relaxometry to obtain information on the bulk crystallinity and crystallization kinetics of the most commercially relevant semi-crystalline polymers. Due to lower signal-to-noise ratios and lower static B_0 homogeneities relative to high field NMR, a pulse sequence based on a magic sandwich echo (MSE) and a CPMG echo train was selected and optimized in terms of pulse timings and acquisition durations to obtain high numerical stability and robustness. In the first part, we studied the temperature-dependent relaxation behavior and identified $T = T_g + 100$ K as the minimum temperature with respect to T_g for which the mobility contrast between crystalline and amorphous protons is sufficient for an unambiguous determination of polymer crystallinity using the chosen decay decomposition approach. More elaborated NMR techniques such as double quantum (DQ) filtering might allow to

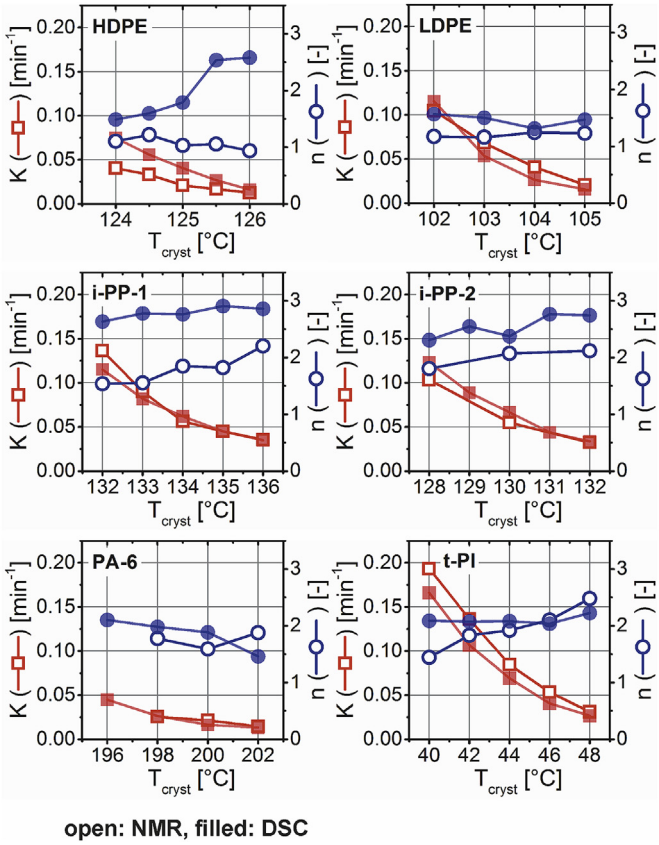

Fig. 12. Avrami rate K and exponent n for isothermal crystallization experiments of different polymers measured by DSC (filled symbols) and NMR (open symbols). For each polymer, the values for the rate K showed a good level of agreement between NMR and DSC. On the other hand, the obtained values for the exponent n were somewhat different for DSC and NMR. The origin of this discrepancy is probably the temperature gradient of ~1 K across the sample in the NMR experiments, which led to a growth rate distribution and therefore an apparently lower n value (see Supporting Information for the isothermal DSC data).

differentiate between crystalline and amorphous protons at even lower temperatures. The obtained bulk crystallinities were compared to DSC and XRD data, and showed good agreement for all polymers within an estimated relative error of ±10% for the respective methods.

In the second part, we focused on the determination of crystallization kinetics, i.e., monitoring of isothermal crystallization, which required a robust design of the pulse sequence, precise temperature calibration, and careful data analysis. We found the combination of a mixed magic sandwich echo (MSE) with a short acquisition duration $\tau_{initial} = 25$ µs followed by a CPMG echo train with short pulse timings $\tau_{CPMG} = 25$ µs to be the most suitable sequence for crystallization experiments as the inherent refocusing properties of the 180° pulse quantitatively select the mobile/amorphous protons. In addition, a CPMG-based approach has the advantage that it is more versatile because of its applicability to low B_0 homogeneity magnets. Two different methods of data analysis were evaluated. A direct approach for which every back-extrapolated CPMG intensity was compared to the MSE maximum at each point in crystallization time, and an indirect approach for which the back-extrapolated CPMG intensities were compared to the initial CPMG intensity of the super-cooled melt. The indirect data analysis was found to be more robust because it relies only on the analysis of CPMG data and is independent of the MSE efficiency. When compared to isothermal DSC experiments, a quantitative analysis using the Avrami model showed good agreement for the average growth rate K, but deviations in the exponent n were seen that were presumably caused by the larger temperature gradients in the current NMR set-up.

Generally, low-field ^{1}H NMR relaxometry is an absolute method for the determination of polymer crystallinity. However, for polymers such as polyethylene that have a high mobility in the crystalline domains, a lower effective crystallinity value might be obtained that can nonetheless still be calibrated using polymer standards or crystallinity values obtained by other techniques such as DSC. In conclusion, benchtop ^{1}H NMR relaxometry was successfully employed to obtain information on the bulk crystallinity and crystallization kinetics of polymers, which opens up the possibility to use this technique in research labs, quality control, or processing labs. Compared to DSC, ^{1}H NMR relaxometry is better suited to the study of slow crystallizations as it does not require peak integration. Furthermore, the non-destructive nature of ^{1}H NMR relaxometry allows for the performance of *in-situ* experiments in combination with applied flow or pressure to achieve better insight into how these parameters affect polymer crystallization [28,29].

Acknowledgements

The authors thank Dr. T. Beskers, J. Leinweber (both PSS, Mainz, Germany) for GPC measurements and Dr. M. Parkinson (Borealis, ExxonMobil) for ^{13}C NMR experiments. We also thank Dr. G. Cavusoglu for XRD experiments, H. Hörig for DSC measurements, and Dr. J. Kübel for proofreading the manuscript. The project was financially supported by the German Research Foundation within the instrumental facility Pro^{2}NMR. We gratefully acknowledge funding of the Bruker D8 through the Helmholtz Energy Materials Characterization Platform (HEMCP) initiated by the Helmholtz Association. M. B. Özen thanks the Ministry of National Education of the Republic of Turkey for financial support.

Appendix A. Supplementary data

Supplementary data related to this article can be found at https://doi.org/10.1016/j.polymer.2018.04.066.

References

[1] J.E. Mark, Physical Properties of Polymers Handbook, Springer, 2007.
[2] D.W. Van Krevelen, K. Te Nijenhuis, in: Properties of Polymers: Their Correlation with Chemical Structure; Their Numerical Estimation and Prediction from Additive Group Contributions, Elsevier, Amsterdam, 2009.
[3] I.M. Ward, J. Sweeney, Mechanical Properties of Solid Polymers, John Wiley & Sons, Chichester, 2012.
[4] Y. Olivier, D. Niedzialek, V. Lemaur, W. Pisula, K. Müllen, U. Koldemir, J.R. Reynolds, R. Lazzaroni, J. Cornil, D. Beljonne, 25th anniversary article: high-mobility hole and electron transport conjugated polymers: how structure defines function, Adv. Mater. 26 (2014) 2119–2136.
[5] A. O'Halloran, F. O'malley, P. McHugh, A review on dielectric elastomer actuators, technology, applications, and challenges, J. Appl. Phys. 104 (2008) 1–10.
[6] B.S. Lalia, V. Kochkodan, R. Hashaikeh, N. Hilal, A review on membrane fabrication: structure, properties and performance relationship, Desalination 326 (2013) 77–95.
[7] U. Gedde, Polymer Physics, Springer, Dordrecht, 1999.
[8] B. Wunderlich. Macromolecular Physics, Academic Press, New York, 1976.
[9] L. Mandelkern, Crystallization of polymers, in: Equilibrium Concepts, Cambridge University Press, Cambridge (UK), 2002.
[10] L. Mandelkern, Crystallization of Polymers, in: Kinetics and mechanisms, Cambridge University Press, Cambridge (UK), 2004.
[11] G. Reiter, G.R. Strobl, Progress in Understanding of Polymer Crystallization, Springer, Berlin, 2007.
[12] E. Piorkowska, G.C. Rutledge, Handbook of Polymer Crystallization, John Wiley & Sons, Hoboken, 2013.
[13] R.H. Somani, L. Yang, L. Zhu, B.S. Hsiao, Flow-induced shish-kebab precursor structures in entangled polymer melts, Polymer 46 (2005) 8587–8623.

[14] G.Z. Papageorgiou, D.S. Achilias, D.N. Bikiaris, G.P. Karayannidis, Crystallization kinetics and nucleation activity of filler in polypropylene/surface-treated SiO_2 nanocomposites, Thermochim. Acta 427 (2005) 117–128.
[15] A.E. Woodward, Atlas of Polymer Morphology, first ed., Hanser, Munich, 1988.
[16] L.E. Alexander, X-ray Diffraction Methods in Polymer Science, Wiley-Interscience, New York, 1970.
[17] F.J. Baltá-Calleja, C.G. Vonk. X-ray Scattering of Synthetic Polymers, Elsevier, Amsterdam, 1989.
[18] G. Kister, G. Cassanas, M. Vert, Effects of morphology, conformation and configuration on the IR and Raman spectra of various poly (lactic acid) s, Polymer 39 (1998) 267–273.
[19] B. Wunderlich, Thermal analysis of Polymeric Materials, Springer Science & Business Media, 2005.
[20] A.T. Lorenzo, M.L. Arnal, J. Albuerne, A.J. Müller, DSC isothermal polymer crystallization kinetics measurements and the use of the Avrami equation to fit the data: guidelines to avoid common problems, Polym. Test. 26 (2007) 222–231.
[21] F. Quinn Jr., L. Mandelkern, Thermodynamics of crystallization in high polymers: poly-(ethylene), J. Am. Chem. Soc. 80 (1958) 3178–3182.
[22] G. Strobl, From the melt via mesomorphic and granular crystalline layers to lamellar crystallites: a major route followed in polymer crystallization? Eur. Phys. J. E 3 (2000) 165–183.
[23] B. Blümich, F. Casanova, S. Appelt, NMR at low magnetic fields, Chem. Phys. Lett. 477 (2009) 231–240.
[24] K. Meyer, S. Kern, N. Zientek, G. Guthausen, M. Maiwald, Process control with compact NMR, Trends Anal. Chem. 83 (2016) 39–52.
[25] A. Adams, Analysis of solid technical polymers by compact NMR, Trends Anal. Chem. 83 (2016) 107–119.
[26] B. Blümich, J. Perlo, F. Casanova, Mobile single-sided NMR. Prog, Nucl. Magn. Reson. Spectrosc 52 (2008) 197–269.
[27] V. Räntzsch, M. Wilhelm, G. Guthausen, Hyphenated low-field NMR techniques: combining NMR with NIR, GPC/SEC and rheometry, Magn. Reson. Chem. 54 (2016) 494–501.
[28] K.-F. Ratzsch, C. Friedrich, M. Wilhelm, Low-field rheo-NMR: a novel combination of NMR relaxometry with high end shear rheology, J. Rheol. 61 (2017) 905–917.
[29] V. Räntzsch, M.B. Özen, K.-F. Ratzsch, G. Guthausen, M. Wilhelm, Low-field RheoNMR: newly developed combination of rheology and time domain (TD)-NMR to correlate mechanical properties with molecular dynamics in polymer melts, AIP Conf. Proc. 1914 (2017) 1–5.
[30] H. Todt, G. Guthausen, W. Burk, D. Schmalbein, A. Kamlowski, Water/moisture and fat analysis by time-domain NMR, Food Chem. 96 (2006) 436–440.
[31] H. Todt, G. Guthausen, W. Burk, D. Schmalbein, A. Kamlowski, Time-domain NMR in quality control: standard application in food, in: Modern Magnetic Resonance, Springer, Berlin, 2006, pp. 1717–1721.
[32] W. Derbyshire, M. Van den Bosch, D. Van Dusschoten, W. MacNaughtan, I. Farhat, M. Hemminga, J. Mitchell, Fitting of the beat pattern observed in NMR free-induction decay signals of concentrated carbohydrate–water solutions, J. Magn. Reson. 168 (2004) 278–283.
[33] V.M. Litvinov, M. van Duin, Real-time 1H NMR relaxation study of EPDM vulcanization, Kautsch. Gummi Kunstst. 55 (2002) 460–463.
[34] K. Saalwächter, B. Herrero, M.A. Lopez-Manchado, Chain order and cross-link density of elastomers as investigated by proton multiple-quantum NMR, Macromolecules 38 (2005) 9650–9660.
[35] A. Papon, K. Saalwächter, K. Schaler, L. Guy, F. Lequeux, H. Montes, Low-field NMR investigations of nanocomposites: polymer dynamics and network effects, Macromolecules 44 (2011) 913–922.
[36] G. Guthausen, V. Räntzsch, C. Biquet, S. Schlabach, M. Wilhelm, Investigation of polymer-filler interactions in tio_2-filled poly (n-alkyl methacrylates) by low-field NMR relaxometry, Macromol. Chem. Phys. 215 (2014) 851–858.
[37] K. Fujimoto, T. Nishi, R. Kado, Multiple-pulse nuclear magnetic resonance experiments on some crystalline polymers, Polym. J. 3 (1972) 448–462.
[38] R. Kitamaru, F. Horii, NMR approach to the phase structure of linear polyethylene, in: Polymer Chemistry, Springer, 1978, pp. 137–178.
[39] K. Bergmann, Determination of polymer crystallinity from proton solid-echo NMR measurements, Polym. Bull. 5 (1981) 355–360.
[40] K. Packer, J. Pope, R. Yeung, M. Cudby, The effects of morphology on ^{1}H NMR spectra and relaxation in semicrystalline polyolefins, J. Polym. Sci., Part B: Polym. Phys. 22 (1984) 589–616.
[41] R. Eckman, P. Henrichs, A. Peacock, Study of polyethylene by solid state NMR relaxation and spin diffusion, Macromolecules 30 (1997) 2474–2481.
[42] P. Kristiansen, E. Hansen, B. Pedersen, Phase distribution during isothermal crystallization of polyethylene probed by solid-state proton NMR free induction decay, J. Phys. Chem. B 103 (1999) 3552–3558.
[43] V.M. Litvinov, J.P. Penning, Phase composition and molecular mobility in nylon 6 fibers as studied by proton NMR transverse magnetization relaxation, Macromol. Chem. Phys. 205 (2004) 1721–1734.
[44] A. O. C. Society, Solid Fat Content (SFC) by Low-resolution Nuclear Magnetic Resonance—the Direct Method. Cd 16b–93 Ed, American Oil Chemists Society, 1997.
[45] A. O. C. Society, Solid Fat Content (SFC) by Low-resolution Nuclear Magnetic Resonance—the Indirect Method. Cd 16–81 Ed, American Oil Chemists Society, 2009.
[46] D. Dadayli, R.K. Harris, A.M. Kenwright, B.J. Say, M.M. Sünnetçioğlu, Solid-state 1 H nmr studies of polypropylene, Polymer 35 (1994) 4083–4087.
[47] G. Feio, J. Cohen-Addad, NMR approach to the kinetics of polymer crystallization. 1. Cis-1, 4-polybutadiene, J. Polym. Sci., Part B: Polym. Phys. 26 (1988) 389–412.
[48] G. Feio, G. Buntinx, J. Cohen-Addad, NMR Approach to the kinetics of polymer crystallization. II. Polydimethylsiloxane solutions, J. Polym. Sci., Part B: Polym. Phys. 27 (1989) 1–24.
[49] E.W. Hansen, P.E. Kristiansen, B. Pedersen, Crystallinity of polyethylene derived from solid-state proton NMR free induction decay, J. Phys. Chem. B 102 (1998) 5444–5450.
[50] P. Kristiansen, E. Hansen, B. Pedersen, Phase distribution in polyethylene versus temperature probed by solid-state proton NMR free induction decay, Polymer 41 (2000) 311–321.
[51] P. Kristiansen, E. Hansen, B. Pedersen, Isothermal crystallization of polyethylene monitored by in situ NMR and analyzed within the “Avrami” model framework, Polymer 42 (2001) 1969–1980.
[52] H. Tanaka, T. Nishi, Real-time measurement of crystallization process of polymers by pulsed nuclear magnetic resonance, J. Appl. Phys. 59 (1986) 1488–1492.
[53] H. Tanaka, T. Nishi, Study of crystallization process of polymer from melt by a real-time pulsed NMR measurement, J. Chem. Phys. 85 (1986) 6197–6209.
[54] K. Takegoshi, C.A. McDowell, A magic echo pulse sequence for the high-resolution nmr-spectra of abundant spins in solids, Chem. Phys. Lett. 116 (1985) 100–104.
[55] D.E. Demco, R. Fechete, B. Blümich, Residual dipolar couplings of soft solids by accordion magic sandwich, Chem. Phys. Lett. 375 (2003) 406–412.
[56] A. Maus, C. Hertlein, K. Saalwächter, A robust proton NMR method to investigate hard/soft ratios, crystallinity, and component mobility in polymers, Macromol. Chem. Phys. 207 (2006) 1150–1158.
[57] C. Wilson, G. Pake, Nuclear magnetic resonance determination of degree of crystallinity in two polymers, J. Polym. Sci. 10 (1953) 503–505.
[58] N. Fuschillo, E. Rhian, J. Sauer, Nuclear magnetic resonance and crystallinity in polyethylene, J. Polym. Sci. 25 (1957) 381–384.
[59] J. Van Vleck, The dipolar broadening of magnetic resonance lines in crystals, Phys. Rev. 74 (1948) 1168–1183.
[60] K. Schmidt-Rohr, H.-W. Spiess, Multidimensional Solid-state NMR and Polymers, Academic Press Limited, London, 1994.
[61] G.E. Pake, Nuclear resonance absorption in hydrated crystals: fine structure of the proton line, J. Chem. Phys. 16 (1948) 327–336.
[62] M.H. Levitt, Spin Dynamics - Basis of Nuclear Magnetic Resonance, Wiley, 2008.
[63] G. Parker, Expansion theorems for magnetic-resonance line shapes, Phys. Rev. B 2 (1970) 2453–2459.
[64] G. Parker, F. Lado, Calculation of NMR line shapes in calcium fluoride from modified moment expansions, Phys. Rev. B 9 (1974) 22–28.
[65] A. Abragam, Principles of Nuclear Magnetic Resonance, Oxford Science Publications, Oxford, 1989.
[66] N. Bloembergen, E.M. Purcell, R.V. Pound, Relaxation effects in nuclear magnetic resonance absorption, Phys. Rev. 73 (1948) 679–712.
[67] R. Kimmich, NMR - Tomography Diffusometry Relaxometry, Springer Verlag, Berlin, 1997.
[68] G. Zimmer, M. Helmle, M. Mehring, F. Rachdi, Lattice-Dynamics and 13C paramagnetic shift in K4C60, Europhys. Lett. 27 (1994) 543–548.
[69] G. Zimmer, M. Mehring, C. Goze, F. Rachdi, Rotational-Dynamics of C60(4-) and electronic excitation in Rb4C60, Phys. Rev. B 52 (1995) 13300–13305.
[70] P.W. Anderson, P.R. Weiss, Exchange narrowing in paramagnetic resonance, Rev. Mod. Phys. 25 (1953) 269–276.
[71] K.J. Fritzsching, K. Mao, K. Schmidt-Rohr, Avoidance of density anomalies as a structural principle for semicrystalline polymers: the importance of chain ends and chain tilt, Macromolecules 50 (2017) 1521–1540.
[72] H.Y. Carr, E.M. Purcell, Effects of diffusion on free precession in nuclear magnetic resonance experiments, Phys. Rev. 94 (1954) 630–638.
[73] S. Meiboom, D. Gill, Modified spin-echo method for measuring nuclear relaxation times, Rev. Sci. Instrum. 29 (1958) 688–691.
[74] W.-G. Hu, C. Boeffel, K. Schmidt-Rohr, Chain flips in polyethylene crystallites and fibers characterized by dipolar ^{13}C NMR, Macromolecules 32 (1999) 1611–1619.
[75] R. Bärenwald, Y. Champouret, K. Saalwächter, K. Schäler, Determination of chain flip rates in poly (ethylene) crystallites by solid-state low-field 1H NMR for two different sample morphologies, J. Phys. Chem. B 116 (2012) 13089–13097.
[76] R. Bärenwald, S. Goerlitz, R. Godehardt, A. Osichow, Q. Tong, M. Krumova, S. Mecking, K. Saalwächter, Local Flips and Chain Motion in polyethylene crystallites: a comparison of melt-crystallized samples, reactor powders, and nanocrystals, Macromolecules 47 (2014) 5163–5173.
[77] M. Hürlimann, D. Griffin, Spin dynamics of Carr–Purcell–Meiboom–Gill-like sequences in grossly inhomogeneous B_0 and B_1 fields and application to NMR well logging, J. Magn. Reson. 143 (2000) 120–135.
[78] M. Avrami, Granulation, phase change, and microstructure kinetics of phase change. III, J. Chem. Phys. 9 (1941) 177–184.